Dynamic and Thermal Analysis of Rotor Drop on Sleeve Type Catcher Bearings in Magnetic Bearing Systems

Xiao Kang
Mechanical Engineering,
Texas A&M University,
College Station, TX 77843
e-mail: kangxiao1990@tamu.edu

Alan Palazzolo
Fellow ASME
James J. Cain Professor I
Mechanical Engineering,
Texas A&M University,
College Station, TX 77843
e-mail: a-palazzolo@tamu.edu

The catcher bearing (CB) is a crucial part of the magnetic bearing system. It can support the rotor when the magnetic bearing is shut down or malfunctioning and limit the rotor's position when large vibration occurs. The sleeve bearing has the advantages of a relatively large contact surface area, simple structure, and an easily replaced surface. There are already many applications of the sleeve type CBs in the industrial machinery supported by the magnetic bearings. Few papers though provide thorough investigations into the dynamic and thermal responses of the sleeve bearing in the role of a CB. This paper develops a coupled two-dimensional (2D) elastic deformation—heat transfer finite element model of the sleeve bearing acting as a CB. A coulomb friction model is used to model the friction force between the rotor and the sleeve bearing. The contact force and 2D temperature distribution of the sleeve bearing are obtained by numerical integration. To validate the finite element method (FEM) code developed by the author, first, the mechanical and thermal static analysis results of the sleeve bearing model are compared with the results calculated by the commercial software SOLIDWORKS SIMULATION*. Second, the transient analysis numerical results are compared with the rotor drop test results in reference. Additionally, this paper explores the influences of different surface lubrication conditions, different materials on rotor-sleeve bearing's dynamic and thermal behavior. This paper lays the foundation of the fatigue life calculation of the sleeve bearing and provides the guideline for the sleeve type CB design.* [DOI: 10.1115/1.4037666]

Keywords: catcher bearing, plane strain, reverse whirl, magnetic bearing

Introduction

The active magnetic bearing (AMB) has been widely used in the industrial fields because it can provide nonfriction, oil free working conditions. The catcher bearing (CB) is a crucial part in the AMB system because it can not only support the rotor when the AMB fails but protect the AMB from being impacted when the rotor has large vibration.

When the AMB fails due to the power supply failure or other issues, the rotor will drop with a high rotational speed and impact the catcher bearing system intensively. During such process, the significant contact force and the thermal power caused by the friction may impair the CB and even the AMB. This result may include plastic deformations, subsurface initiated spalling, and thermal abrasion wear, and all these will lead to severe noise, vibration, and even damage of the entire AMB system. Thus, it is essential to analyze the dynamic and thermal behavior of the rotor and the CB system during rotor's drop process. Only in this way the proper approaches of the CB design can be found so as to minimize not only the impact force but also the induced heating and prolong the fatigue life of the CB.

Numerous researchers have modeled or tested the ball bearing type CB. Gelin et al. [1] analyzed the dynamic behavior of flexible rotor drop onto the catcher bearing, while the coulomb friction was neglected. Ishii and Kirk simulated the transient response of the rotor dropping onto the CB in 1991 with a Jeffcott rotor model, and the optimal damping was selected to prevent the reverse whirl [2]. Sun et al. [3] developed a detail ball bearing model in 2003 and added the one-dimensional thermal model in 2006 [4]. Lee and Palazzolo [5] developed the nonlinear ball bearing model where the rain flow counting method was used to calculate the catcher bearing fatigue life. Wilkes et al. [6] modeled the axial friction between the rotor flange and the axial face of the ball bearing type catcher bearing. The axial friction was believed to induce the forward whirl when the vertical arranged rotor dropped onto the catcher bearing. All the aforementioned researchers were committed to establish the high-fidelity model of the catcher bearing and the rotor, such that both the dynamic responses and the thermal behaviors of each component can be considered.

Most of the literature focuses on ball bearing type catcher bearing. Actually, other bearing types, such as the sleeve type catcher bearing by WAUKESHA's rotor de-levitation system, are also used in industries and thus investigated by engineers [7]. There are also some researchers who have investigated sleeve type catcher bearing. In 1995, Swanson et al. numerically [8] and experimentally [8,9] analyzed rotor drop onto a sleeve type catcher bearing. Parametric studies including the lubrication conditions, imbalance, support conditions, and catcher bearing types, and Swanson et al. concluded that lower imbalance, better lubrication, and soft support were recommended for the catcher bearing design. Wilkes and Allison numerically and experimentally analyzed the multicontact dry-friction whip and whirl [10]; such research involves the contact model between the rotor and the stator, which is similar as the contact between the rotor and the catcher bearing.

Contributed by the Structures and Dynamics Committee of ASME for publication in the JOURNAL OF ENGINEERING FOR GAS TURBINES AND POWER. Manuscript received July 3, 2017; final manuscript received July 10, 2017; published online October 3, 2017. Editor: David Wisler.

However, literatures are quite scarce about the detailed modeling of sleeve type catcher bearing related to the rotordynamics, thermodynamics, and their coupled relationship. For the thermal analysis, most of the literature simplifies the catcher bearing race as a one-dimensional lumped mass and fail to calculate the temperature distribution around the surface which will under predict the peak temperature. This paper provides the detailed dynamic and thermal analyses of the rotor drop onto the sleeve type catcher bearing. In this paper, the rotor is modeled by the six-degrees-of-freedom Timoshenko beam element and the sleeve type catcher bearing is analyzed with the two-dimensional (2D) plane strain model. Moreover, the deformation of the bearing cross section is analyzed, by assuming that the penetration between the rotor and sleeve bearing is uniform during contacting along the axial direction. The dynamic response and the 2D temperature distribution in the cross section of the sleeve bearing during rotor drop are obtained. The thermal expansion due to the temperature variation is also considered. The Stribeck friction model is used to model the friction between rotor and sleeve bearing. Two steps of validation are designed to justify the proposed finite element method (FEM) analysis, first, both the mechanical and thermal static analysis results of the sleeve bearing model are compared with the results calculated by the commercial software SOLIDWORKS SIMULATION, and second, the transient analysis numerical results are compared with the test results obtained by Swanson et al. [8].

Then, different parameters such as dynamic friction coefficient, sleeve bearing material, and imbalance are analyzed to study their influence on the rotordynamics after the rotor drops onto the sleeve type CB. This research establishes the preliminary model for the fatigue life prediction of the sleeve bearing and provides practical recommendations for the sleeve type catcher bearing design.

Sleeve Bearing Finite Element Model

The sleeve type catcher bearing is modeled by the plane strain model. Here, the variation in axial direction is ignored [11]. The deformation in the cross section is analyzed. The four-node quadrilateral element is used to model the sleeve bearing. Figure 1 shows the mesh of the sleeve bearing's cross section. The nodes located outside of the surface of the sleeve bearing are supported by the radial and tangential springs as shown in Fig. 1.

In the plane strain model, the relationship between strain and stress is as shown in the below equation [11]:

$$\underline{\boldsymbol{\sigma}} = \underline{\mathbf{E}}\,\underline{\boldsymbol{\varepsilon}} \tag{1}$$

where $\underline{\boldsymbol{\sigma}} = [\sigma_{11} \quad \alpha_{22} \quad \sigma_{12}]^{\mathrm{T}}$, $\underline{\boldsymbol{\varepsilon}} = [\varepsilon_{11} \quad \varepsilon_{22} \quad \varepsilon_{12}]^{\mathrm{T}}$.

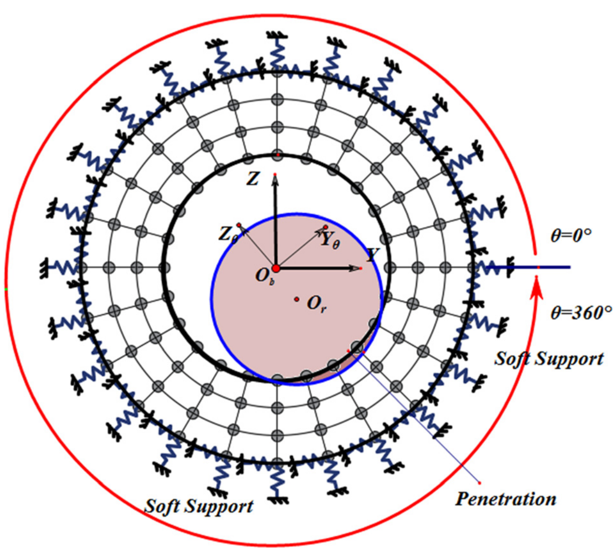

Fig. 1 Plane strain model of the sleeve bearing

The material matrix in plane strain model is shown by the below equation:

$$\underline{\mathbf{E}}^e = \frac{E}{(1+v)(1-2v)}\begin{bmatrix} 1-v & v & 0 \\ v & 1-v & 0 \\ 0 & 0 & \dfrac{1-2v}{2} \end{bmatrix} \tag{2}$$

Since the four-node quadrilateral element is used, the element stiffness matrix can be obtained as [11]

$$\mathbf{K}^e = t^e \int_{\Omega_e} (\mathbf{B}^e)^T \mathbf{E}^e \mathbf{B}^e d\boldsymbol{\Omega}_e \tag{3}$$

where $\underline{B}^e$ is the matrix in $\underline{\varepsilon}^e = \underline{B}^e \underline{u}^e$, $\underline{u}^e$ is the nodal displacement of the element, and $\underline{\varepsilon}^e$ is the strain of the element. The mass matrix is as shown in below equation:

$$\underline{\mathbf{M}}^e = t^e \int_{\Omega_e} \rho (\mathbf{N}_e)^T \mathbf{N}_e d\boldsymbol{\Omega}_e \tag{4}$$

where $\underline{N}_e$ is the shape function matrix of the four-node quadrilateral element.

The geometry of the element is mapped from its actual shape into a square. By using the Gauss quadrature method, the element stiffness matrix can be obtained as

$$\underline{\mathbf{K}}^e \approx \hat{t}^e \sum_{s=1}^{n_G} \sum_{t=1}^{n_G} w_s w_t \mathbf{B}_e{}^T \mathbf{E}_e \mathbf{B}_w \det(\mathbf{J}_e) \tag{5}$$

The element mass matrix can also be obtained as

$$\underline{\mathbf{M}}^e \approx \hat{t}^e \sum_{s=1}^{n_G} \sum_{t=1}^{n_G} w_s w_t \rho \mathbf{N}_s{}^T \mathbf{N}_w \det(\mathbf{J}_e) \tag{6}$$

where $\hat{t}^e$ is the thickness of the sleeve bearing in the axial direction. After constructing the nodal connectivity matrix, the mesh plot can be obtained as shown in Fig. 2.

The global stiffness and mass matrix are assembled based on the nodal connectivity and the nodal constraint. The proportional

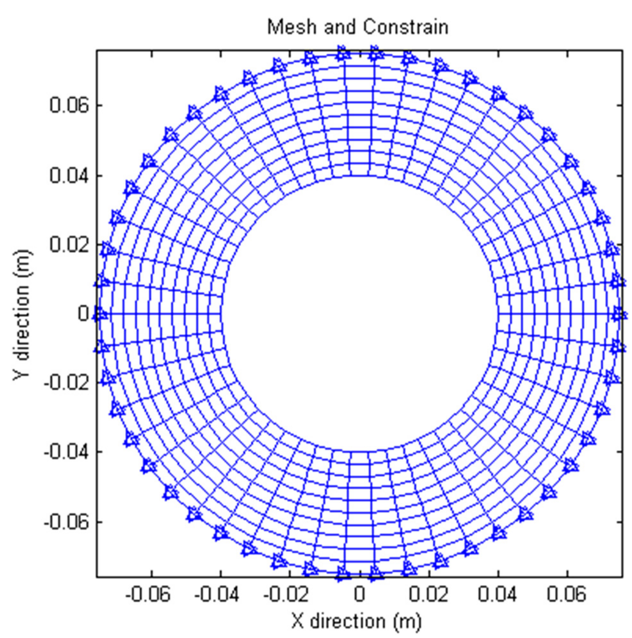

Fig. 2 Mesh check in MATLAB for the plane strain model of the sleeve bearing

damping is added to the sleeve bearing model. The coefficients with respect to mass matrix and stiffness matrix are calculated based on the measured damping coefficient at two different frequencies. The two frequencies are the upper bound and lower bound of its operation frequencies to guarantee the calculated damping is a conservative value [11]

$$\underline{\mathbf{C}} = \alpha_M \underline{\mathbf{M}} + \alpha_K \underline{\mathbf{K}} \tag{7}$$

where the coefficients α_M and α_K can be calculated as

$$\begin{bmatrix} \alpha_M \\ \alpha_K \end{bmatrix} = \begin{bmatrix} 1 & {\omega_1}^2 \\ 1 & {\omega_2}^2 \end{bmatrix}^{-1} \begin{bmatrix} 2\omega_1\zeta_1 \\ 2\omega_2\zeta_2 \end{bmatrix} \tag{8}$$

Sleeve Bearing Thermal Model

The governing equation for the transient heat transfer in the plane system is

$$C_T\rho\frac{dT}{dt} - \frac{\partial}{\partial x}\left(k_x\frac{\partial T}{\partial x}\right) - \frac{\partial}{\partial y}\left(k_y\frac{\partial T}{\partial y}\right) + \beta(T - T_\infty) = \widehat{q}_n \tag{9}$$

where k_x and k_y are thermal conductivities (in W/(m °C)) along the x and y directions. β is the convective heat transfer coefficient. After obtaining the weak form, substitute the finite element approximation as

$$T = \sum_{j=1}^{n} T_j^e N_j^e \tag{10}$$

The finite element model is obtained as

$$\sum_{j=1}^{n} C_T M_{ij}\dot{T}_j^e + \sum_{j=1}^{n}(K_{ij}^e + H_{ij}^e)T_j^e = F_i^e + P_i^e \tag{11}$$

The element stiffness matrix can be formed as

$$K_{ij}^e = \int_{\Omega_e}\left(k_x\frac{\partial N_i^e}{\partial x}\frac{\partial N_j^e}{\partial x} + k_y\frac{\partial N_i^e}{\partial y}\frac{\partial N_j^e}{\partial y}\right)dxdy \tag{12}$$

The thermal source vector is described as

$$F_i^e = \int_{\Omega_e} fN_i^e dxdy + \oint_{\Gamma_e} q_n^e N_i^e ds = f_i^e + Q_i^e \tag{13}$$

P_i and H_{ij} are the terms related to the heat convection

$$H_{ij} = \beta^e\int_{\Gamma}\psi_i^e\psi_j^e ds \tag{14}$$

$$P_i^e = \beta^e\int_{\Gamma_e}\psi_i^e T_\infty ds \tag{15}$$

When using the four-node isoquadrilateral element, the element stiffness matrix is changed as

$$K_{ij}^e = \int_{-1}^{1}\int_{-1}^{1}\left(k_x\frac{\partial N_i^e}{\partial x}\frac{\partial N_j^e}{\partial x} + k_y\frac{\partial N_i^e}{\partial y}\frac{\partial N_j^e}{\partial y}\right)\det(\mathbf{J})d\zeta d\eta \tag{16}$$

Thus, the element stiffness matrix can be obtained as

$$\mathbf{K}^e = \int_{-1}^{1}\int_{-1}^{1}(k_x\mathbf{H}_x^T\mathbf{H}_x + k_y\mathbf{H}_y^T\mathbf{H}_y)\det(\mathbf{J})d\zeta d\eta \tag{17}$$

Here, $\mathbf{H}_x$ and $\mathbf{H}_y$ can be found in the Appendix.

Then, use the "Gauss quadrature" method to conduct the numerical integration as

$$\mathbf{K}^e = \sum_{s=1}^{n_G}\sum_{s=1}^{n_G}(k_x\mathbf{H}_x^T(\zeta_s,\eta_s)\mathbf{H}_x(\zeta_s,\eta_s) + k_y\mathbf{H}_y(\zeta_s,\eta_s)^T\mathbf{H}_y(\zeta_s,\eta_s))\det(\mathbf{J}) \tag{18}$$

The thermal mass is solved as

$$\mathbf{M}^e = \int_{-1}^{1}\int_{-1}^{1} C_T\rho\mathbf{N}^T\mathbf{N}\det(\mathbf{J})d\zeta d\eta \tag{19}$$

Here, $\mathbf{N}$ is the shape function matrix; C_T is the specific heat; and ρ is the material density.

In the current model, only edge 4-1 (node 4 to node 1 in the local element) in the first layer of the element in radial direction has the heat convection boundary conditions. For those elements, the detailed boundary conditions are as

$$\mathbf{H}_{41}^e = \frac{\beta_{41}^e h_{41}^2}{6}\begin{bmatrix} 2 & 0 & 0 & 1 \\ 0 & 0 & 0 & 0 \\ 0 & 0 & 0 & 0 \\ 1 & 0 & 0 & 2 \end{bmatrix} \tag{20}$$

which will be assembled in the global thermal stiffness matrix. Also, P_i^e, expressed as Eq. (21), will be assembled into the global thermal load vectors

$$\mathbf{P}_i^e = \frac{\beta_{41}^e T_\infty h_{41}^e}{2}\begin{bmatrix} 1 \\ 0 \\ 0 \\ 1 \end{bmatrix} \tag{21}$$

The heat power generated by the friction between the surfaces of the rotor and the sleeve bearing will be explained in the section Contact Model Between Rotor and Sleeve Bearing.

Thermal Expansion Calculation

The procedure described in this section calculates the thermal load caused by thermal expansion. Those thermal loads will be applied on the nodes of each element. Ignoring the axial deformation, the thermal stress in the plane strain model can be evaluated as

$$\underline{\boldsymbol{\sigma}}_0 = \frac{-E\alpha\Delta T}{1-2v}\begin{bmatrix} 1 & 1 & 0 \end{bmatrix}^{\mathrm{T}} \tag{22}$$

In plane strain model, the material matrix is shown as Eq. (2).

Assuming the bearing is under uniform expansion and without angular distortions, the thermal stress is

$$\underline{\boldsymbol{\sigma}}_0 = \frac{-E\alpha\Delta T}{1-2v}\begin{bmatrix} 1 & 1 & 0 \end{bmatrix}^{\mathrm{T}} \tag{23}$$

The equation of motion of the sleeve bearing can be derived as

$$\underline{\mathbf{M}}_B\underline{\ddot{\mathbf{X}}}_B + \underline{\mathbf{K}}_B\underline{\mathbf{X}}_B + \underline{\mathbf{C}}_B\underline{\dot{\mathbf{X}}}_B = \underline{\mathbf{F}}_{\text{Thermal}} + \underline{\mathbf{F}}_Q \tag{24}$$

where $\underline{F}_Q$ is the contact load from the rotor.

The thermal load $\underline{\mathbf{F}}_{\text{Thermal}}$ caused by the thermal expansion is calculated as

$$\underline{\mathbf{F}}_{\text{Thermal}} = \int_\Omega \underline{\mathbf{B}}_e{}^T\underline{\mathbf{E}}_e\underline{\boldsymbol{\varepsilon}}_0 d\Omega = \int_\Omega \underline{\boldsymbol{\sigma}}_0\underline{\mathbf{B}}_e d\Omega = \int_\Omega \underline{\boldsymbol{\sigma}}_0\underline{\mathbf{D}}_e\underline{\mathbf{N}}_e d\Omega \tag{25}$$

Using the Gauss quadrature integration, the thermal load can be derived as

Table 1 Material and geometry parameters for sleeve bearing [12]

Young's modulus (GPa)	110
Poisson's ratio	0.33
Density (kg/m^3)	8300
Inner diameter (m)	0.08
Outer diameter (m)	0.15
Mesh in radial direction	10
Mesh in circumferential direction	50

$$\underline{\mathbf{F}}_{\text{Thermal}} = t^e \sum_{s=1}^{n_G} \sum_{t=1}^{nG} w_s w_t \underline{\boldsymbol{\sigma}}_0 \underline{\mathbf{B}}_e(\zeta_{1s}, \zeta_{2t}) \det(\underline{\mathbf{J}}_e(\zeta_{1s}, \zeta_{2t})) \tag{26}$$

which is updated at each time-step based on the temperature variation.

Contact Between Rotor and Sleeve Bearing

The key thing for the rotor drop analysis is to model the contact between the rotor and the sleeve bearing, as shown in Fig. 1.

Here, the rotor is built by the Timoshenko beam model. The equation of motion of the rotor is shown as

$$\underline{\mathbf{M}}_r \ddot{\underline{\mathbf{X}}}_r + [\underline{\mathbf{C}}_r + \Omega \underline{\mathbf{G}}] \dot{\underline{\mathbf{X}}}_r + \underline{\mathbf{K}}_r \underline{\mathbf{X}}_r = \underline{\mathbf{F}}_r \tag{27}$$

where $\underline{M}_r$ is the mass matrix of the rotor, C_r is the damping matrix, $\underline{G}$ is the gyroscopic matrix, and K_r is the shaft stiffness matrix. The vector $\underline{X}_r$ contains the information of the nodal degree-of-freedom. F_r is the load vector including the imbalance force and the nonlinear catcher bearing forces. Ω is the angular velocity of the rotor. Each beam node has six degree-of-freedoms.

The rotor surface is regarded to be rigid. The local radial and tangential penetration of each surface node can be calculated by the coordinate transformation. When contact occurs, the penalty spring is connected between the rotor and surface nodes of the sleeve bearing. The stiffness of the penalty spring is set as 10,000 times larger than the maximum element of the stiffness matrix of the sleeve bearing [12]. The total contact force is the summation of the total force at each node. The local normal contact force for each surface node is as Eq. (28). Note that the contact force can only be calculated when the value of the local radial penetration δ_i is positive; otherwise, they are zero

$$F_{ni} = K_p \delta_i \tag{28}$$

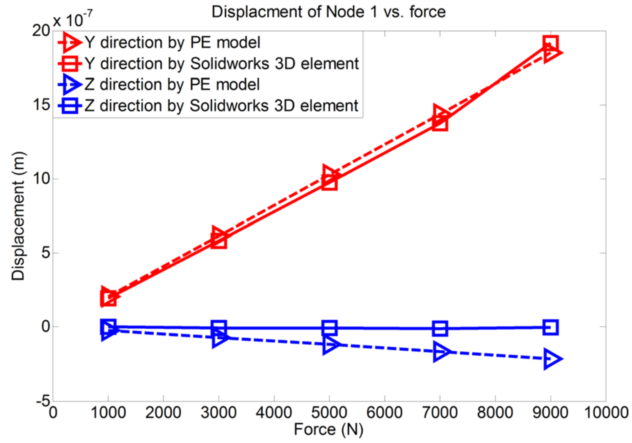

Fig. 4 Displacements of node 1 versus applied force

Table 2 Thermal property for the bronze sleeve bearing [12]

Specific heat (J/kg °C)	380
Thermal conductivity (W/(m °C))	47
Thermal expansion ratio (1/°C)	1.80×10^{-05}
Heat convection coefficient (W/(m °C))	20
Ambient temperature (°C)	25

$$F_{ti} = \mu_{sb} F_{ni} \tag{29}$$

The μ_{sb} can be calculated by the Stribeck friction model as shown in the below equation:

$$\mu_{sb} = -\frac{2}{\pi} \arctan(\varepsilon_f v_{\text{rel}}) \left[\frac{\mu_s - \mu_d}{1 + \delta_f |v_{\text{rel}}|} + \mu_d \right] \tag{30}$$

where v_{rel} is the relative tangential velocity between node i of the sleeve bearing surface and the corresponding rotor contact surface. The parameter ε_f determines the slope of the approximation function. The parameter δ is a positive number that determines the rate at which the static friction coefficient approaches by the dynamic friction coefficient with respect to relative velocity. The term " $-2/\pi \arctan(\varepsilon f v_{\text{rel}})$ " has the same function as the

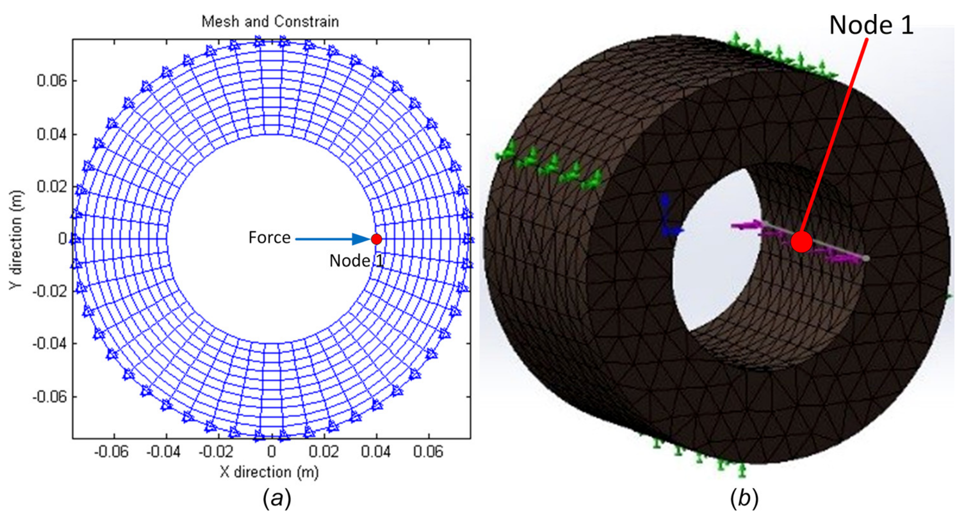

Fig. 3 Mesh, constrain, and force direction (*a*) plane strain model by author and (*b*) SOLIDWORKS three-dimensional (3D) element model

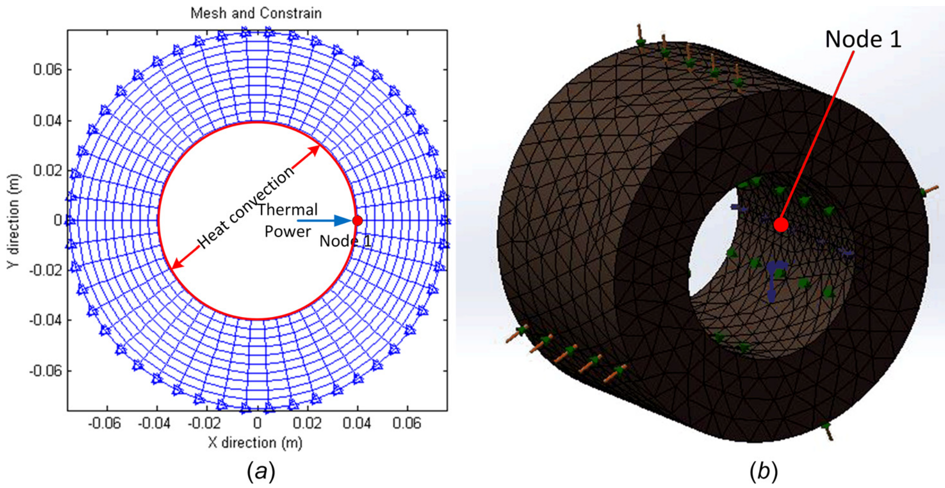

Fig. 5 Mesh, constrain and heat source: (*a*) 2D thermal model by author and (*b*) SOLIDWORKS 3D element model

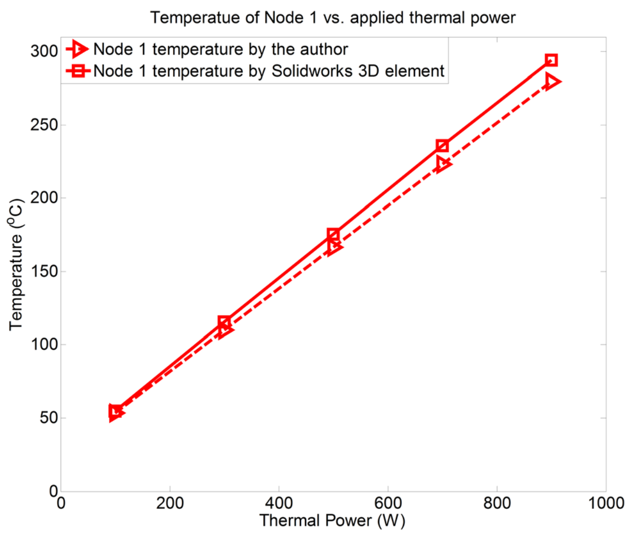

Fig. 6 Temperature of node 1 versus applied heat

"sign" function. But this term, according to Ref. [6], has better performance for the numerical stability and can agree well with the experimental data as well.

The total force act on the rotor can be calculated as

$$\underline{\mathbf{F}}_{\text{total}} = \sum_{i=1}^{n} \underline{\mathbf{T}}_i \underline{\mathbf{F}}_i \tag{31}$$

where

$$\underline{\mathbf{F}}_{\text{total}} = \begin{bmatrix} F_y \\ F_z \end{bmatrix}; \quad \underline{\mathbf{T}}_i = \begin{bmatrix} \cos\theta_i & \sin\theta_i \\ -\sin\theta_i & \cos\theta_i \end{bmatrix}; \quad \underline{\mathbf{F}}_i = \begin{bmatrix} F_{ni} \\ F_{ti} \end{bmatrix}$$

The penetration value δ_i corresponds to each surface node of CB and can be calculated as

$$\delta_i = y_{\text{rotor}} \cos\theta_i + z_{\text{rotor}} \sin\theta_i - \text{clearance} - (y_i \cos\theta_i + z_i \sin\theta_i) \tag{32}$$

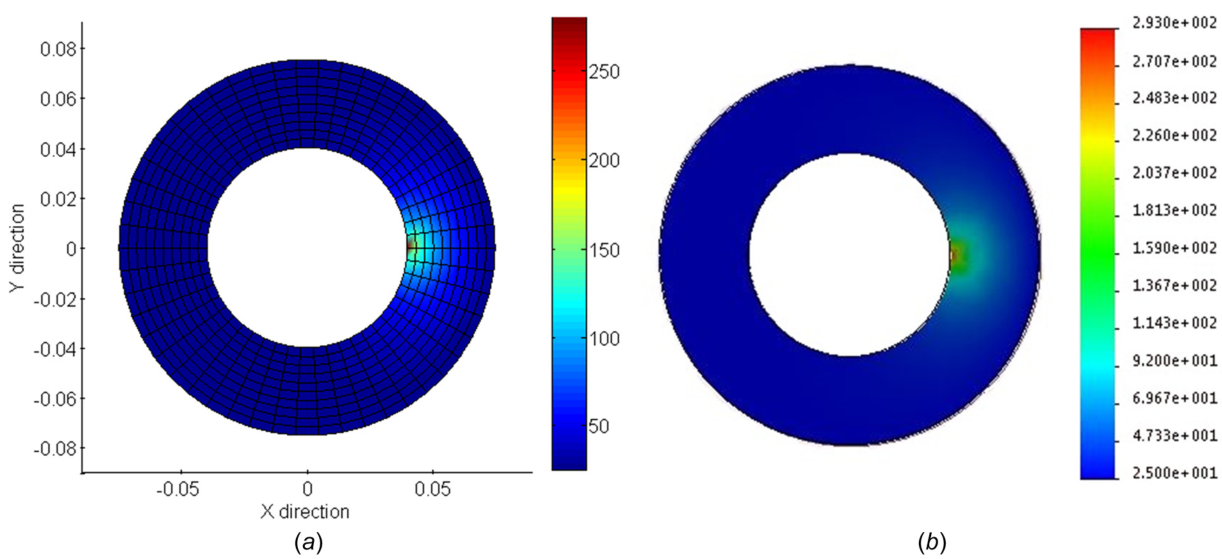

Fig. 7 Temperature distribution when the applied heat power is 900 W: (*a*) 2D FEM thermal model by author and (*b*) 3D FEM model by SOLIDWORKS simulation

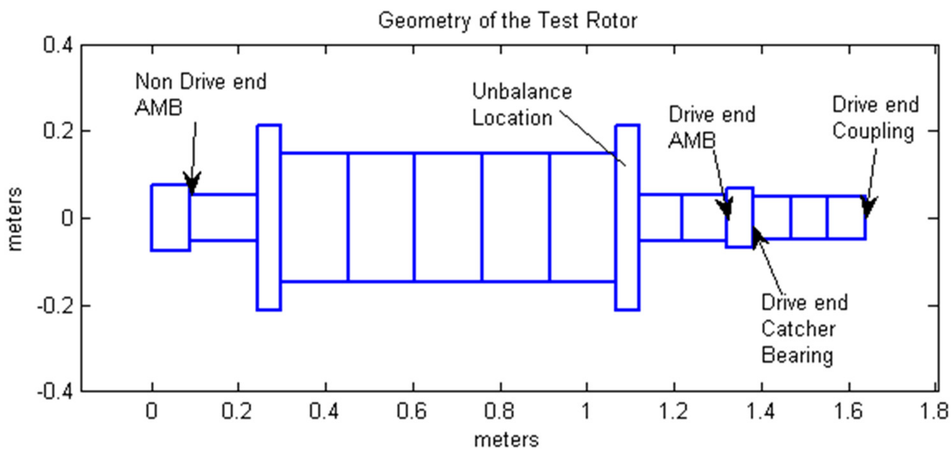

Fig. 8 Rotor geometry in Ref. [8]

The heat power generated from the friction between the rotor and the catcher bearing surface is obtained as

$$P_{fi} = F_{ti} v_{i\text{rel}} \tag{33}$$

The heat power in Eq. (33) will be assembled in the global thermal load vector.

Validation of the Mechanical Model

To validate the plane strain FEM model in this paper, the static analysis results calculated by the author are compared with the results from the SOLIDWORKS mechanical, a widely used commercial software. In the SOLIDWORKS model, the sleeve bearing is constructed as a 3D model which is meshed by the 3D element. Here, the basic geometry and material information of the sleeve bearing is given in Table 1.

In the static analysis, for the plane strain model, a nodal force is applied in the horizontal direction of node 1, as shown in Fig. 3. For the SOLIDWORKS model, the force (with the same direction) is a linear distributed force whose summation is the same as the nodal force in the plane strain model as shown in Fig. 3.

Figure 4 shows the curve about the displacement of the node 1 versus the value of applied force. The dashed lines represents the results from author's plane strain model. The solid lines represents the results from the SOLIDWORKS. The results in Y direction are very close, and the maximum difference is about 3%. It indicates that the direct stiffness of the plane strain model is reliable. There are some difference between the displacement in Z direction, which may be caused by the difference in mesh geometry. Such difference may be reduced by finer mesh. But due to the relatively small value of the displacement, it will not influence much for the dynamic response.

Table 3 Parameters in the 2D numerical model

CB Young's modulus (GPa)	110
CB Poisson's ratio	0.33
CB density (kg/m^3)	8300
CB inner diameter (m)	0.15
CB outer diameter (m)	0.19
CB mesh in radial direction	2
CB mesh in circumferential direction	28
Catcher bearing clearance (mm)	0.25
AMB stiffness (N/m)	7.15×10^6 N/m
AMB damping (N s/m)	1.0×10^4 N s/m
Rotor drop spin speed (rpm)	4000
Catcher bearing proportional damping coefficient	0.01

Validation of the Thermal Model

To validate the thermal model of the sleeve bearing, the static analysis results obtained by the 2D thermal code in this paper are compared with the results calculated by SOLIDWORKS. The thermal conductivity and convection coefficients are shown in Table 2.

A heat source is applied on a node as shown in Fig. 3. A similar linear distributed heat source with the same sum value is applied on the edge of the SOLIDWORKS' 3D model as shown in Fig. 5.

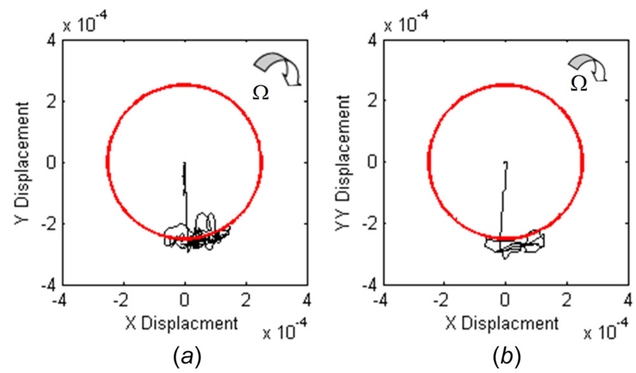

Fig. 9 Rotor drop onto lubricated bronze type sleeve bearing with low imbalance: (*a*) simulation results and (*b*) test results

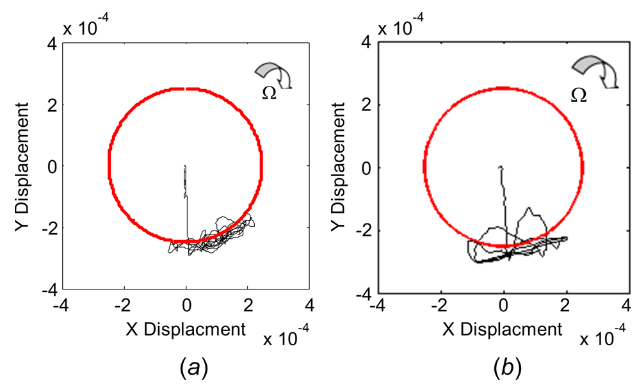

Fig. 10 Rotor drop onto unlubricated bronze type sleeve bearing with low imbalance: (*a*) simulation results and (*b*) test results

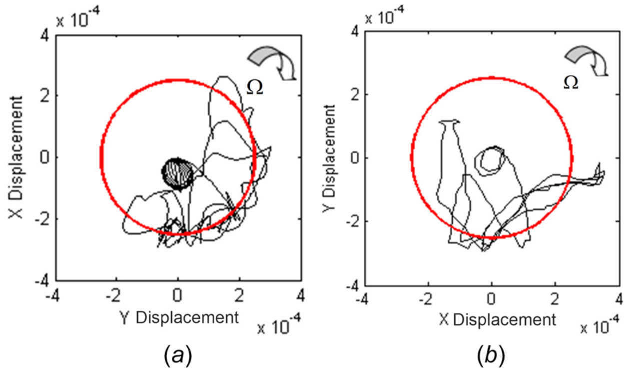

Fig. 11 Rotor drop onto lubricated bronze type sleeve bearing with high imbalance: (*a*) simulation results and (*b*) test results

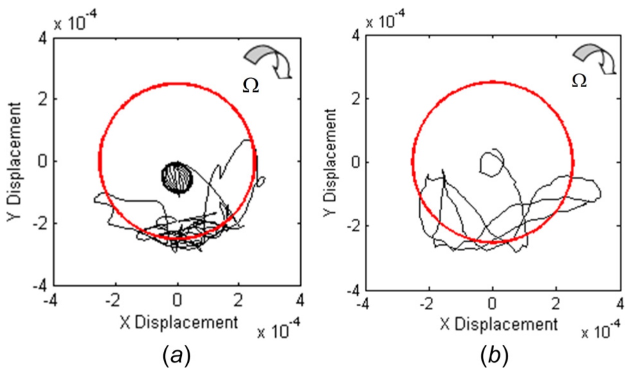

Fig. 12 Rotor drop onto lubricated bronze type sleeve bearing with high imbalance: (*a*) simulation results and (*b*) test results

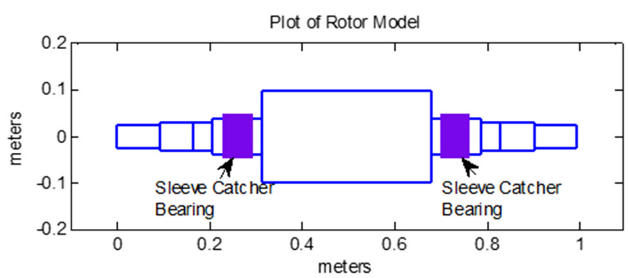

Fig. 13 Rotor geometry and catcher bearing location

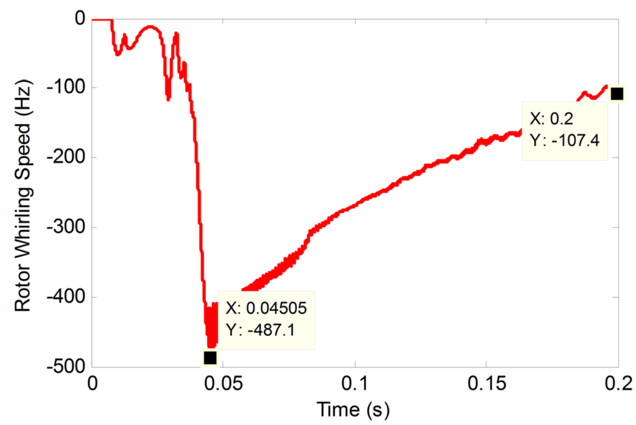

Fig. 15 Rotor whirling speed when the friction coefficient is 0.4

In this validation model, the temperature of the outside boundary is prescribed as the ambient temperature 25 °C. The inner boundary is applied heat convection boundary condition with the convection coefficient of 20 $\mathrm{W/(m^2\,{}^\circ C)}$. Here, the temperature of node 1 in FEM model in this paper is compared with the temperature of the node located at the middle of the edge of applied heat source in the SOLIDWORKS 3D model. The results are shown in Fig. 6.

Figure 6 shows that the plot about maximum temperature versus sum heat power. The red line represent the 2D temperature model in the paper, the blue line shows the results in SOLIDWORKS. The results appear quite similar. Figure 7 shows under the same total heat power, the temperature distribution are similar. The comparison in this section shows that the 2D thermal model in this paper is reliable.

Experimental Validation

The simulation results using the sleeve bearing model in this paper are compared with the experiment data in Ref. [8]. In Ref. [8], Swanson and Kirk carried out a drop test using the test rig which initially aims to simulate a gas turbine compressor section [9]. In this rig, the rotor is supported by two AMBs which are located at node 2 and node 12, as shown in Fig. 8. During the drop test, only the drive end AMB is de-energized while the AMB at the nondrive end is still working.

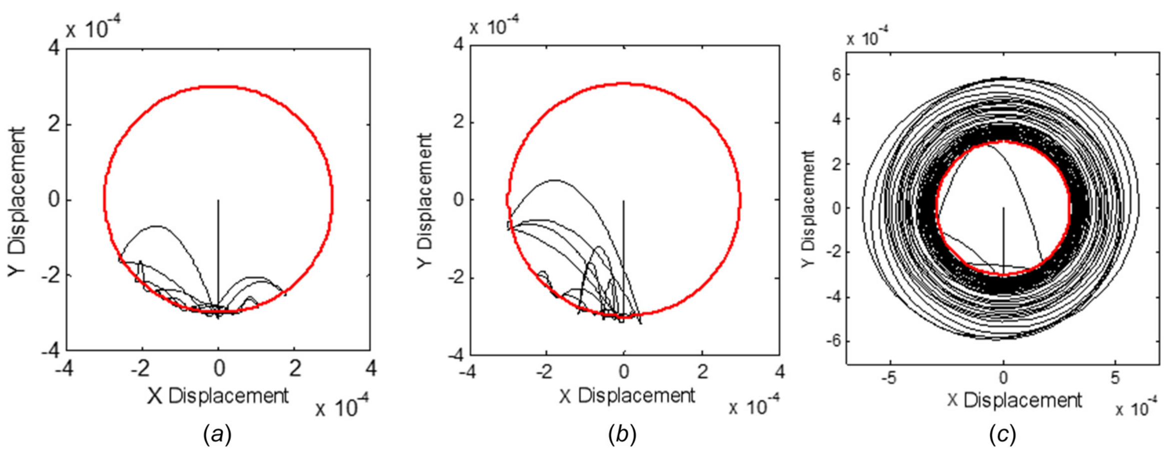

Fig. 14 Rotor orbit with different dynamic friction coefficients

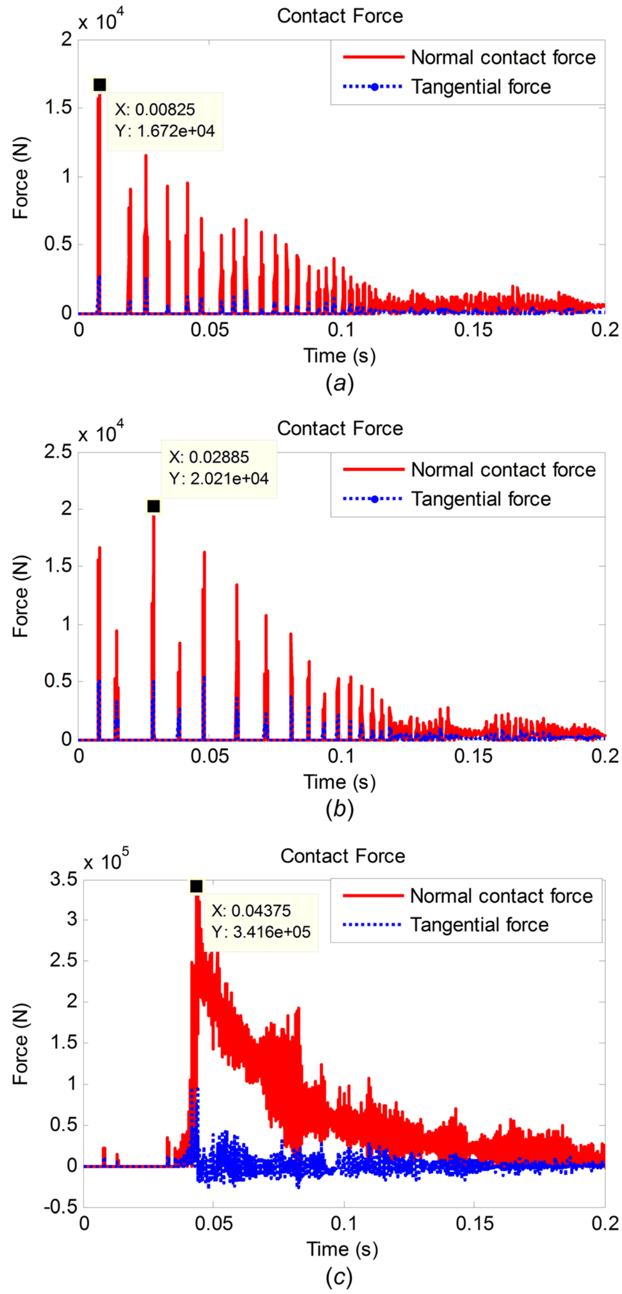

Fig. 16 Contact force with different friction coefficients: (*a*) $\mu_d = 0.15$, (*b*) $\mu_d = 0.3$, and (*c*) $\mu_d = 0.4$

According to Ref. [8], the magnetic bearing stiffness is 7.15×10^6 N/m and the damping is 1×10^4 N s/m, which are obtained by the frequency dependent stiffness and damping curves provided by the manufacturer [8]. The imbalance of the rotor is added on the node 9 as shown in Fig. 8. Swanson et al. tested rotor drop onto lubricated and unlubricated bronze type sleeve bearing. He also did drop tests with or without rotor imbalance. The rotor's rotational direction in the test is clockwise [8].

To compare the test results in Ref. [8], the author develops a dynamic-thermal coupled 2D numerical model based on the test rig information provided by Swanson et al. [8]. The results of the numerical model are compared with the reference's test data. The parameters in the simulation model are shown in Table 3.

For the rotor dropping onto the lubricated bronze sleeve bearing, the dynamic friction coefficient is chosen as 0.15 according to Ref. [8]. The imbalance value is 0.25 kg mm, which is placed on the node 9 of the rotor. The numerical and test results are shown in Fig. 9.

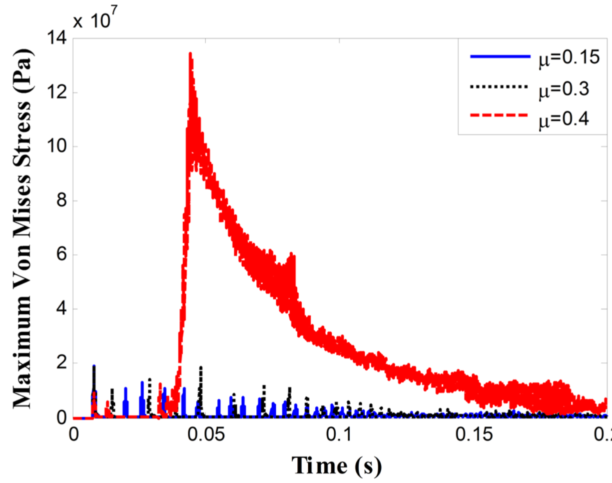

Fig. 17 Maximum von Mises stress time history with different friction coefficients

As shown in Fig. 9, the simulation results and the experiment results have the similar trend that both of the rotors slide on the right side of the bottom of the sleeve bearing after a few bounces. Additionally, there is no reverse or forward whirl.

For the rotor dropping onto the unlubricated bronze sleeve bearing, the dynamic friction coefficient is chosen as 0.3 based on Ref. [8]. The imbalance value is 0.25 kg mm, which is placed at node 9. The numerical and test results are presented in Fig. 10.

According to Fig. 10, when the sleeve bearing is not lubricated, both the simulation and experiment results show that the rotor has a larger vibration compared with the case with lubricated sleeve bearing.

For the rotor dropping onto the unlubricated bronze sleeve bearing with a high imbalance value, the dynamic friction coefficient is chosen as 0.3 according to Ref. [8]. The imbalance value is 2.73 kg mm, which is placed at node 9. The numerical and test results are shown in Fig. 11.

In the simulation, the rotor has the trend of resulting in the reverse whirl, while there is no reverse whirl occurring in the experiment. The difference may be caused by the difficulty in accurately estimating the housing stiffness and the exact friction coefficient.

For the rotor dropping onto the lubricated bronze sleeve bearing with high imbalance value, the dynamic friction coefficient is chosen as 0.15 according to Ref. [8]. The imbalance, with the value of 2.73 kg mm, is placed at node 9. The numerical and test results are shown in Fig. 12.

Generally speaking, the simulation results qualitatively agree with the experiment data from Swanson's paper. Some reasons that may explain the discrepancy include: (1) the friction coefficients that are used as the recommended values by Swanson et al. [8] and have uncertainty, (2) though the sleeve bearing is hard mounted, the housing's flexibility will still influence the penetration and contact force, and (3) the test sensor may not have been exactly located at the catcher bearing's location. Because only one AMB is de-energized, the rotor will have conical motion which will make the penetration looks different if the sensor was not located at the same position as the CB. Swanson et al. provided an excellent benchmark for vibration correlation but did not include contact force and the temperature. Thus, other experiments with the capability of measuring the forces and the temperatures are required for the further validation of the current dynamic-thermal coupled FEM model.

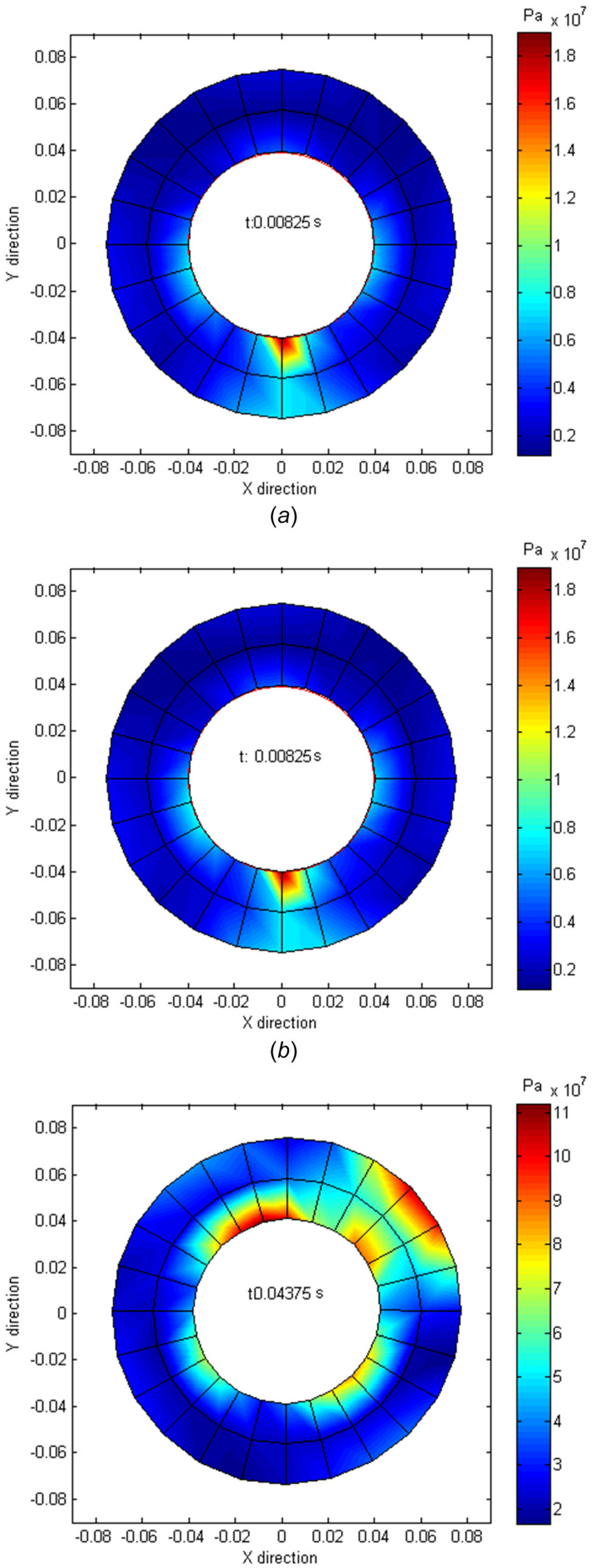

Fig. 18 Von Mises stress distribution when the largest von Mises stress occurs: (*a*) $\mu_d = 0.15$, (*b*) $\mu_d = 0.3$, and (*c*) $\mu_d = 0.4$

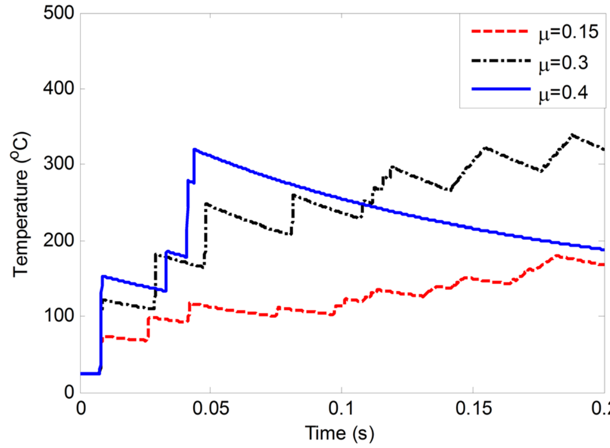

Fig. 19 Time histories of peak temperature with different friction coefficients

Influence of Dynamic Friction Coefficient of the Sleeve Bearing Contact Surface

The influence of the dynamic friction coefficient of the sleeve bearing surface on the rotor drop event is analyzed. Different from the former validation sections, because the transient calculation will spend much simulation time, the mesh density is reduced to 24 in circumferential direction and 2 in radial direction to increase the calculation efficiency. Additionally, the rotor is replaced by a symmetric rotor so as to further reduce the calculation time. The rotor is same as the rotor in Ref. [5]. According to the sensitivity analysis of the mesh density, there will be about 10% difference with the results from SOLIDWORKS in mechanical static analysis. However, it is enough to see the trend of the influences by the friction coefficient. The geometry, material and thermal parameters of the sleeve bearing are shown in Table 1. The stiffness is selected as 4.6×10^7 N/m for each support spring, while the damping for each support spring is chosen as 278 N s/m. The catcher bearing clearance is set to be 0.3 mm in this section. The material of the rotor is steel, and its geometry is shown in Fig. 13. The rotor is 1 m long. The largest diameter is 0.2 m. When the rotor drops, the rotational speed is 10,000 rpm.

The transient simulation period in this simulation is 0.2 s. Let the friction coefficient vary from 0.15 to 0.4. Figure 14 shows the rotor orbits with different friction coefficients. It can be seen that when the friction coefficient rises to 0.4, the rotor starts to have reverse whirl. Then, the penetration becomes very large (0.3 mm).

Figure 15 shows reverse whirl with a coefficient of friction of 0.4. The whirling speed initially reaches about −487.1 Hz and then decays to about −107.4 Hz at 0.2 s. The negative values of the whirling frequencies mean the rotor's whirling direction is against the rotor's spin direction.

Figure 16 shows the time histories of the normal contact forces and the tangential forces with different friction coefficients. When the reverse whirl occurs, the normal contact forces are greatly increased, which can reach more than 10 times of the cases without reverse whirl. The contact force greatly decays when the rotor whirling speed decays for the reverse whirl case. So the high contact forces are caused mainly by the large whirling speed.

Figure 17 shows the time history of the maximum von Mises stress with different friction coefficients. Figure 18 shows the von Mises stress distributions when the peak von Mises stress occurs during the time span. The maximum von Mises stress is seen to dramatically increase when the increased friction coefficient becomes sufficient to induce reverse whirl. The reverse whirl state stress is about 134.2 MPa, which is near the yield stress of the material (144 MPa) [13]. Note the rotor and the CB clearances are the same as those in Ref. [5]. For the sleeve bearing, the

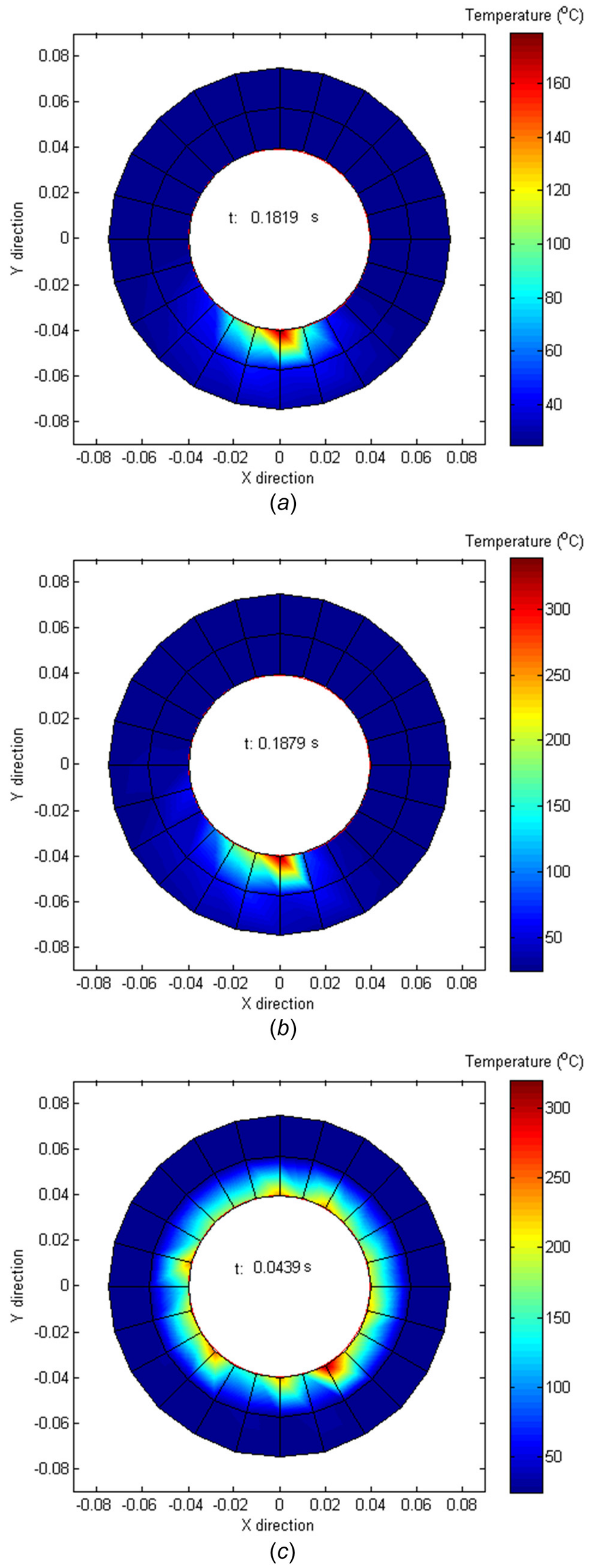

Fig. 20 Temperature distribution with different friction coefficients: (*a*) $\mu_d = 0.15$, (*b*) $\mu_d = 0.3$, and (*c*) $\mu_d = 0.4$

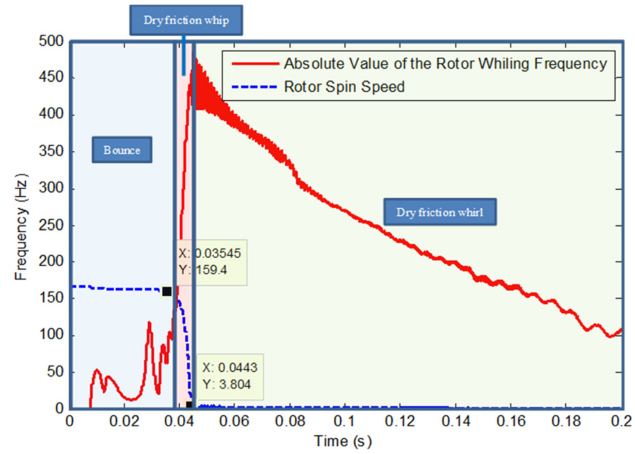

Fig. 21 Rotor whiling frequency and rotor spin speed

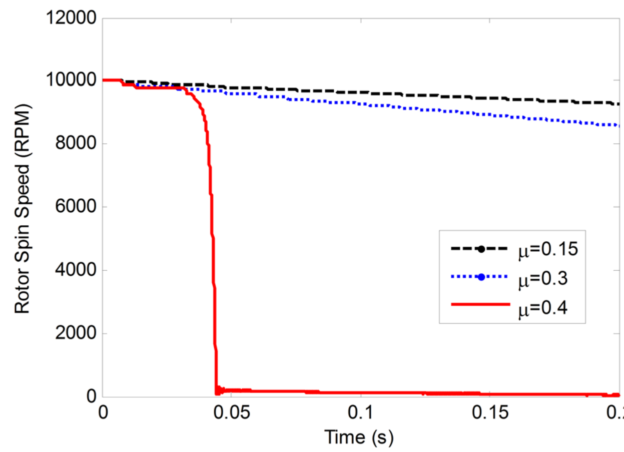

Fig. 22 Rotor spin speeds with different lubrication conditions

Table 4 Material properties

Material properties	Bronze	Stainless steel	Aluminum
Young's modulus (GPa)	110	189.6	71.7
Poisson's ratio	0.33	0.28	0.34
Density (kg/m^3)	8300	7800	2800
Specific heat (J/kg K)	380	477	875
Thermal conductivity (W/(m K))	47	14.9	177
Thermal expansion ratio (1/K)	1.80×10^5	3.91×10^5	7.30×10^4
Friction coefficient (unlubricated)	0.3 [8]	0.5 [14]	0.61 [14]
Support spring stiffness (N/m)	4.6×10^7	4.6×10^7	4.6×10^7
Support spring damping (N s/m)	278	278	278

maximum von Mises stresses are about 18.98 MPa, 18.96 MPa, and 120 MPa, which are much smaller than the stress value (more than 1000 MPa) in Ref. [5] when using ball bearing type CB and under similar lubrication conditions.

Figure 19 shows the time histories of the peak temperature with different friction coefficients. It shows that the temperature increases quickly as the coefficient of friction increases, especially when there is reverse whirl. However, for the reverse whirl case, the sleeve bearing quickly reaches a peak temperature, and then the temperature starts to decay. It is possible that the rotor's rotational speed drops fast and the rotor starts rolling and the friction force will be small when the rolling occurs. For the cases without

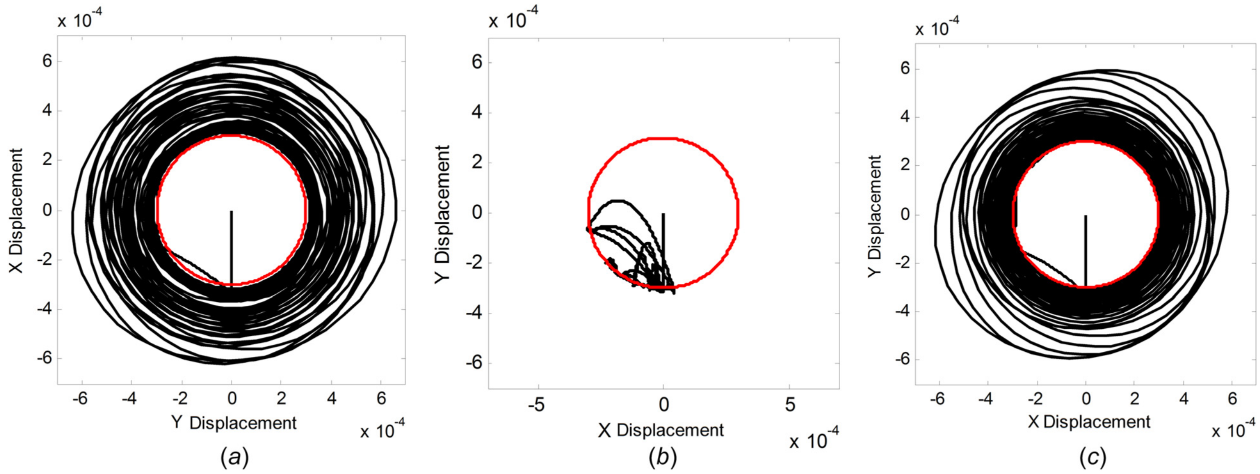

Fig. 23 Rotor orbits with different materials, (*a*) aluminum, (*b*) bronze, (*c*) steel

reverse whirl, the rotor's spin speed decays slowly and the rotor is sliding on the sleeve bearing surface. This will generate more heat than the rolling condition. It can be seen in Fig. 19 that the temperatures for the sleeve bearings without reverse whirl continue to increase and gradually exceed the peak temperature in the case with reverse whirl.

Figure 20 shows the temperature distribution when the sleeve bearing reaches to the peak temperature during the first 0.2 s transient period under different lubrication conditions. It can be seen that when there is no reverse whirl, the peak temperature increases with the friction coefficient and the highest temperature occurs around the contact zone. When reverse whirl happens, the temperature is almost evenly distributed.

In Fig. 21, the red line represents the absolute value of the rotor whirling frequency, and the blue line shows the rotor's spin speed. These two lines enable the calculation of the velocity of the contact point between the rotor and the catcher bearing and the ratio between the rotor whirling frequency and the rotor's spin speed. From the ratio and the velocity, we can find there are three steps in the reverse whirl conditions. They are bounce, dry friction whip, and dry friction whirl. From Fig. 17, it can be seen that the higher von Mises stress occurs after 0.0443 s, which is in the dry friction whirl process. It is because the high whiling frequency results in a high centrifugal force and results in the high von Mises stress. From Fig. 19, the temperature increases before 0.0443 s, which is in the bounce and dry friction whirl processes. Because before 0.0443 s, the sliding friction dominates the contact between the rotor and CB, which will generate large heat, while after 0.0443 s, the rotor mainly rolls on the CB without slipping and such process will generate limited heat and have limited influence on the CB's temperature.

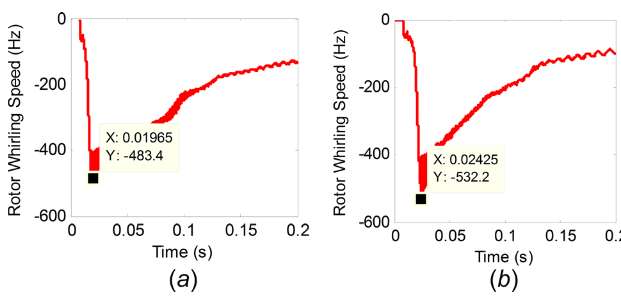

Fig. 24 Rotor whiling speed, (*a*) aluminum, (*b*) steel

Figure 22 shows the rotor spin speeds with different lubrication conditions. It can be seen that with larger friction coefficients, the rotor spin speeds will decay faster, especially when there is a reverse whirl. It is because the large friction forces caused by the dry friction whip will greatly reduce the rotor's spin speed.

Influence of Sleeve Bearing Material

Three types of commonly used materials are simulated to investigate their influences on the rotor drop event. These materials include stainless steel, bronze, and aluminum. Their mechanical and thermal properties are shown in Table 4. Here, the dynamic friction coefficients are selected based on Refs. [8] and [14]. All the materials are assumed to be unlubricated. Here, the friction coefficient of the aluminum CB is 0.61, while the friction coefficients of the steel CB and the bronze CB are 0.5 and 0.3 [8,14], respectively.

Figure 23 shows the rotor orbits with three different catcher bearing materials. It can be seen that reverse whirl occurs for the aluminum and steel type sleeve bearings, due to their relatively large friction coefficients. Figure 21 shows that aluminum has the largest maximum penetration which is 0.338 mm, while for bronze, the maximum penetration is only 0.0187 mm.

Figure 24 shows the variations of the whirling speeds of the aluminum and steel. It can be seen that both of them have negative whirling speeds. They first reach a very high peak value and then start to decay, with the peak whirling speed of the steel (532.2 Hz) being higher than the aluminum (483.4 Hz). Note such whirling speeds are much larger than the rotor's rotational spin speed (166.7 Hz).

Figure 25 shows the normal contact force with different catcher bearing materials. It shows that the steel type CB has the largest maximum normal contact force which is 1.905×10^6 N, while the maximum normal contact forces of the aluminum and the bronze type CB are 3.854×10^5 N and 2.021×10^4 N, respectively.

The time histories of the von Mises stresses with different materials are shown in Fig. 26. It can be seen that, similar as the contact force, the steel CB has the highest peak von Mises stress during the simulation transient time period, and the bronze type CB has the lowest von Mises stress because it does not generate the reverse whirl. The maximum von Mises stresses of the aluminum and the steel CB are 150 MPa and 250 MPa. Both of them surpass their yield stresses, 137 MPa and 206 MPa, respectively [14].

Figure 27 shows the von Mises stress distribution when the maximum von Mises stress is occurring. It can be seen that the

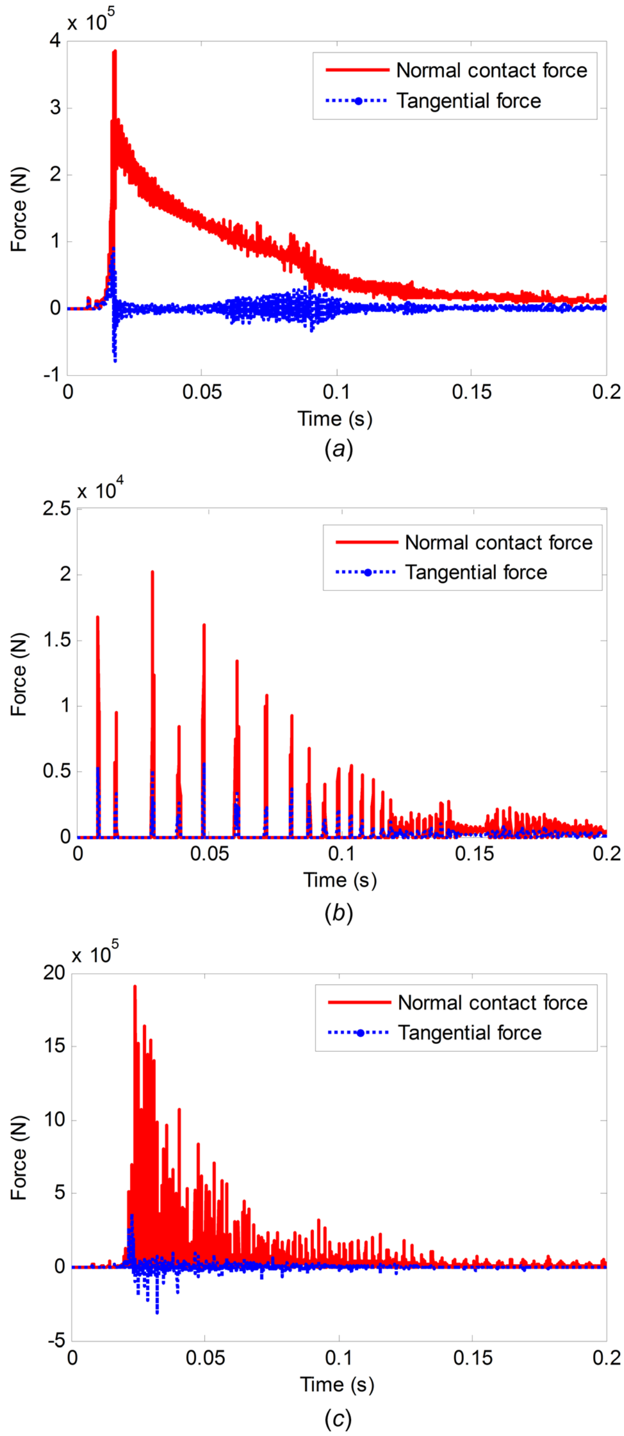

Fig. 25 Normal contact force with different materials: (*a*) aluminum, (*b*) bronze, and (*c*) steel

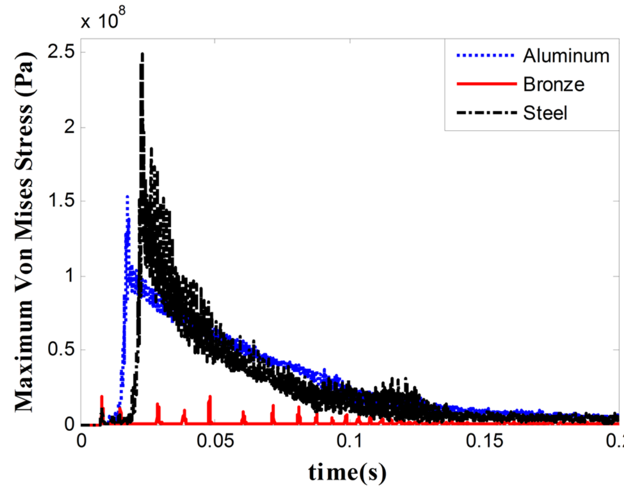

Fig. 26 Maximum von Mises stress time history with different materials

steel has the largest von Mises stress. The bronze CB has the lowest von Mises stress because there is no reverse whirl. It shows that the higher von Mises stress levels extend beyond the immediate contact area due to vibration and deformation of the sleeve bearing.

Figure 28 shows the variations of the peak temperatures with different materials. The aluminum temperature is higher than bronze and steel during the first few hits. This is because the aluminum CB has the highest friction coefficient which induces reverse whirl. Additionally, it has the lowest thermal mass. Therefore, it can generate more heat power during contact and the temperature can also rise quicker. With the same heat convection boundary condition, the aluminum CB has a higher cooling rate which may be caused by its relatively low thermal mass. The bronze has the lowest peak temperature in the first few hits. However, due to the sliding friction and the relatively concentrated contact area, its peak temperature gradually increases and surpasses the peak temperatures of the aluminum and steel CB. Its cooling rate is higher than the steel CB and lower than the aluminum CB.

Figure 29 shows the temperature distributions when the peak temperature in the 0.2 s transient period occurs for different materials. It can be seen that without the reverse whirl, the peak temperature usually occurs on the bottom of the sleeve bearing. The nodes, which have been impacted by the rotor, also have relatively higher temperatures. When there is reverse whirl, the temperature is about evenly distributed.

From the earlier discussion, the unlubricated bronze CB does not generate the reverse whirl, so it has the lowest normal contact force and von Mises stress. However, due to its sliding friction and the concentrated contact area, it gradually gets the highest peak temperature among these three materials. Both aluminum and steel CB cases exhibit reverse whirl and have high contact force and von Mises stress. Thus, it can be seen that without lubrication, bronze performs better for this catcher bearing simulation study as compared with steel and aluminum. Currently, all the friction coefficients in the earlier discussion are selected based on Refs. [8] and [14].

Conclusions

The dynamic and thermal responses of the sleeve type catcher bearing during the rotor drop event are analyzed. The bearing is constructed by the 2D plane strain model. The 2D heat transfer model is also integrated. Additionally, the thermal load, which is caused by the thermal expansion, is updated at each time-step based on the temperature variation. For the drop analysis, the rotor is represented by a Timoshenko beam model. The temperature distributions and von Mises stress distributions are predicted. The model is validated and compared with the experimental data from Ref. [8]. The influences of different lubrication conditions, sleeve bearing materials are analyzed. The results provide the following findings:

(1) The computation results qualitatively agree with the test data from Swanson et al.

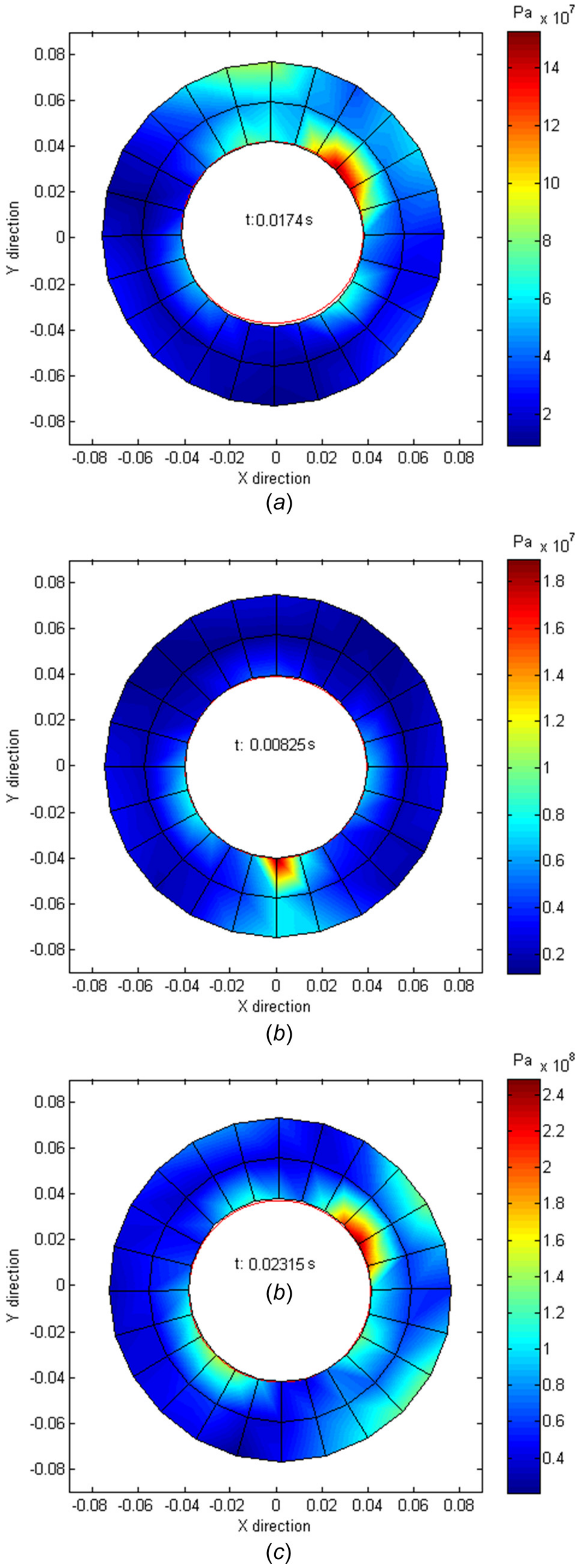

Fig. 27 Maximum von Mises stress with different materials: (*a*) aluminum, (*b*) bronze, and (*c*) steel

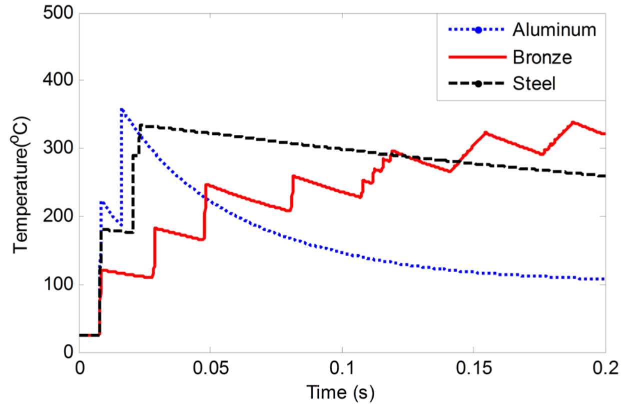

Fig. 28 Variation of the peak temperature with different materials under unlubricated conditions

(2) When there is no reverse whirl, the areas with higher temperatures are all located near the contact points. When there is reverse whirl, the temperature is nearly evenly distributed.

(3) Higher friction coefficients will result in higher contact force and von Mises stress. When there is reverse whirl, there are three steps for the rotor's motion: bouncy, dry friction whip, and dry friction whirl. The reverse whirl may lead to higher stress than the material's yield stress in the simulation cases.

(4) The occurrence of reverse whirl does not necessarily cause higher peak temperatures than cases without reverse whirl. The normal contact force is very high but the friction force in rolling contact is relatively low and there is no slip, during pure rolling contact reverse whirl. Thus, the generated heat may less than in the sliding friction cases without reverse whirl.

(5) By comparing the three types of unlubricated materials (stainless steel, bronze, and aluminum), we found that using the stainless steel material can result in the highest normal contact force and von Mises stress. It is because it has the highest Young's modulus and a relatively high friction coefficient (0.5). Additionally, with the same heat convection boundary condition, due to its higher thermal mass, the steel sleeve bearing has the lowest cooling rate. The aluminum sleeve CB has the highest peak temperature in the first few hits but its cooling rate is also the highest. This may result from having the lowest thermal mass. The bronze sleeve CB's cooling rate is in the middle among the three materials considered and it also has the lowest peak von Mises stress according to the simulation results. Thus, the bronze has the best performance for this application. This conclusion should be viewed with knowledge that the simulation results were very sensitive to the friction coefficient, which typically has considerable uncertainty. The friction coefficients in this paper are based on Refs. [8] and [14]. Friction coefficients vary due to machining quality and environmental conditions; thus, the final design of the CB for a given application should consider the material, machining, and environment, and include a reasonable uncertainty in the friction coefficient.

The fatigue life calculated by the stress cycle and material S-N curve will be analyzed in a future paper. Additionally, sometimes the bearing will fail due to the extremely high local temperature such as in the thermal abrasion wear effect. Because the 2D temperature distribution has been obtained, the thermal abrasion wear will be included to improve the fatigue life prediction of the sleeve bearing.

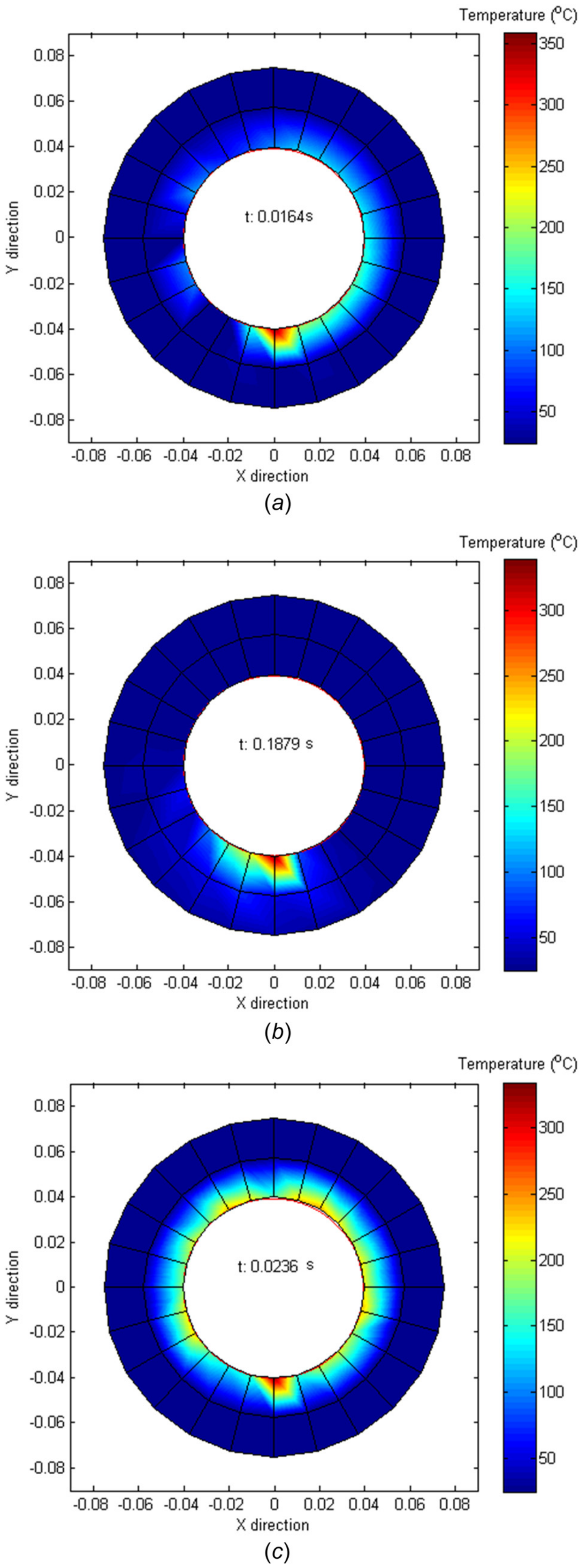

Fig. 29 Temperature distribution with different materials: (*a*) aluminum, (*b*) bronze, and (*c*) steel

Acknowledgment

This research was supported by the Turbomachinery Research Consortium (TRC) at Texas A&M University.

Nomenclature

AMB = active magnetic bearing
CB = catcher bearing
E = Young's modulus
$\underline{\mathbf{E}}$ = material matrix
h_{41} = length of the element edge from node 4 to 1
J_e = Jacobian matrix
$\mathbf{N}$ = element shape function
t = catcher bearing thickness
v = Poisson ratio
v_{irel} = relative velocity between rotor and bearing
α = thermal expansion ratio
β = heat convection coefficient
δ = penetration
$\underline{\varepsilon}$ = strain vector
ζ_i = damping coefficient under frequency no i
$\underline{\sigma}_0$ = thermal stress
ω_i = frequency no i
Ω = rotational speed

Appendix

Calculation of $\mathbf{H}_x$ and $\mathbf{H}_y$ in Eq. (17)

$$\mathbf{H}_x = \frac{\partial \mathbf{N}}{\partial x} = \begin{bmatrix} \frac{\partial N_1}{\partial x} \\ \frac{\partial N_2}{\partial x} \\ \frac{\partial N_3}{\partial x} \\ \frac{\partial N_4}{\partial x} \end{bmatrix} = \begin{bmatrix} 1 & 0 & 0 & 0 & 0 & 0 & 0 & 0 \\ 0 & 0 & 1 & 0 & 0 & 0 & 0 & 0 \\ 0 & 0 & 0 & 0 & 1 & 0 & 0 & 0 \\ 0 & 0 & 0 & 0 & 0 & 0 & 1 & 0 \end{bmatrix}$$

$$\times \begin{bmatrix} \underline{J}_{2\times 2}^{-1} & 0 & 0 & 0 \\ 0 & \underline{J}_{2\times 2}^{-1} & 0 & 0 \\ 0 & 0 & \underline{J}_{2\times 2}^{-1} & 0 \\ 0 & 0 & 0 & \underline{J}_{2\times 2}^{-1} \end{bmatrix} \begin{bmatrix} \frac{\partial N_1}{\partial \zeta} \\ \frac{\partial N_1}{\partial \eta} \\ \frac{\partial N_2}{\partial \zeta} \\ \frac{\partial N_2}{\partial \eta} \\ \frac{\partial N_3}{\partial \zeta} \\ \frac{\partial N_3}{\partial \eta} \\ \frac{\partial N_4}{\partial \zeta} \\ \frac{\partial N_4}{\partial \eta} \end{bmatrix}$$

$$\mathbf{H}_y = \frac{\partial \mathbf{N}}{\partial y} = \begin{bmatrix} \frac{\partial N_1}{\partial y} \\ \frac{\partial N_2}{\partial y} \\ \frac{\partial N_3}{\partial y} \\ \frac{\partial N_4}{\partial y} \end{bmatrix} = \begin{bmatrix} 0 & 1 & 0 & 0 & 0 & 0 & 0 & 0 \\ 0 & 0 & 0 & 1 & 0 & 0 & 0 & 0 \\ 0 & 0 & 0 & 0 & 0 & 1 & 0 & 0 \\ 0 & 0 & 0 & 0 & 0 & 0 & 0 & 1 \end{bmatrix}$$

$$\times \begin{bmatrix} \underline{J}_{2\times2}^{-1} & 0 & 0 & 0 \\ 0 & \underline{J}_{2\times2}^{-1} & 0 & 0 \\ 0 & 0 & \underline{J}_{2\times2}^{-1} & 0 \\ 0 & 0 & 0 & \underline{J}_{2\times2}^{-1} \end{bmatrix} \begin{bmatrix} \frac{\partial N_1}{\partial \zeta} \\ \frac{\partial N_1}{\partial \eta} \\ \frac{\partial N_2}{\partial \zeta} \\ \frac{\partial N_2}{\partial \eta} \\ \frac{\partial N_3}{\partial \zeta} \\ \frac{\partial N_3}{\partial \eta} \\ \frac{\partial N_4}{\partial \zeta} \\ \frac{\partial N_4}{\partial \eta} \end{bmatrix}$$

References

[1] Gelin, A., Pugnet, J. M., and Hagopian, J. D., 1990, "Dynamic Behavior of Flexible Rotors With Active Magnetic Bearings on Safety Auxiliary Bearings," Third International Conference on Rotor Dynamics, Lyon, France, Sept. 10–12, pp. 503–508.

[2] Ishii, T., and Kirk, R. G., 1996, "Transient Response Technique Applied to Active Magnetic Bearing Machinery During Rotor Drop," ASME J. Vib. Acoust., **118**(2), pp. 154–163.

[3] Sun, G., Palazzolo, A., Provenza, A., and Montague, G., 2004, "Detailed Ball Bearing Model for Magnetic Suspension Auxiliary Service," J. Sound Vib., **269**(3), pp. 933–963.

[4] Sun, G., 2006, "Rotor Drop and Following Thermal Growth Simulations Using Detailed Auxiliary Bearing and Damper Models," J. Sound Vib., **289**(1), pp. 334–359.

[5] Lee, J. G., and Palazzolo, A., 2012, "Catcher Bearing Life Prediction Using a Rainflow Counting Approach," ASME J. Tribol., **134**(3), p. 031101.

[6] Wilkes, J., Moore, J., Ransom, D., and Vannini, G., 2013, "An Improved Catcher Bearing Model and an Explanation of the Forward Whirl/Whip Phenomenon Observed in Active Magnetic Bearing Transient Drop Experiments," ASME J. Eng. Gas Turbines Power, **136**(4), p. 042504.

[7] Penfield, S. R., Jr., and Rodwell, E., 2001, "Auxiliary Bearing Design Considerations for Gas Cooled Reactors," International Atomic Energy Agency, Palo Alto, CA, Report No. IAEA-TECDOC–1238.

[8] Swanson, E. E., Raju, K. V. S., and Kirk, R. G., 1996, "Test Results and Numerical Simulation of AMB Rotor Drop," Sixth International Conference on Vibrations in Rotating Machine, Sept. 9–12, pp. 119–131.

[9] Swanson, E. E., and Kirk, R. G., 1995, "AMB Rotor Drop Initial Transient on Ball and Solid Bearings," Magnetic Bearings, Magnetic Drives and Dry Gas Seals, Conference & Exhibition (MAG), Alexandria, VA, Aug. 10–11, pp. 227–235.

[10] Wilkes, J. C., and Allison, T. A., 2015, "General Model for Two-Point Contact Dry-Friction Whip and Whirl: Further Advancements and Experimental Test Results," ASME Paper No. GT2015-43815.

[11] Palazzolo, A., 2016, *Vibration Theory and Applications With Finite Elements and Active Vibration Control*, Wiley, Chichester, UK.

[12] Reddy, J. N., 2005, *Finite Element Method*, 3rd ed., McGraw-Hill, New York.

[13] Oberg, E., Jones, F. D., Horton, H. L., and Ryffel, H. H., 1990, *Machinery's Handbook*, 23rd ed., Industrial Press, New York.

[14] Norton, R. L., 1994, *Machine Design: An Integrated Approach*, Prentice-Hall, Upper Saddle River, NJ.